Ag_2S nanoheaters with multiparameter sensing for reliable thermal feedback during in vivo tumor therapy

Yingli Shen, [1,*] Harrisson Santos,[2,*], Erving Ximendes, [1,3*], Ana Sanz-Portilla,[1] Luis Monge,[1,3] Nuria Fernández,[1,3] Carlos Jacinto,[2] Carlos Brites,[4] Luis Dias Carlos,[4] Antonio Benayas,[1,3] M. Carmen Iglesias-de la Cruz,[1,3] and Daniel Jaque.[1,3]

[1] *Fluorescence Imaging Group, Universidad Autónoma de Madrid, 28049, Madrid, Spain*

[2] *Grupo de Fotônica e Fluidos Complexos, Instituto de Física, Universidade Federal de Alagoas, 57072-900, Maceió-AL, Brazil*

[3] *Nanobiology Group, Instituto Ramón y Cajal de Investigación Sanitaria. Ctra. Colmenar Viejo, km. 9100 28034 Madrid, Spain*

[4] *Departamento de Física and CICECO—Aveiro Institute of Materials, University of Aveiro, 3810-193, Aveiro, Portugal*

E-mail: daniel.jaque@uam.es

Abstract

The irruption of luminescent nanothermometry in biomedicine has enabled achievements that were considered to be outside the reach of conventional techniques. Such achievements would include, for instance, controlled *in vivo* thermal therapies of tumors allowed by the combination of thermosensitive and heating properties in a single nanostructure. However, the reliability of intratumoral thermal readings is in question due to the presence of artefacts caused by the peculiar optical properties of biological tissues. In this work, we demonstrate how it is possible to perform precisely *in vivo* intratumoral thermal reading during therapy. The method we propose is based on the use of heating nanoparticles (NPs) capable of multiparametric thermal sensing. We demonstrate how the convergence of the different thermal readouts becomes a solid indicator of their reliability as contactless thermal sensors. This new method has been demonstrated using NIR-II emitting Ag_2S NPs as self-monitored photothermal agents (S-MPThs) offering over 90% light-to-heat conversion efficiency together with high sensitivity multiparametric thermal sensing through the spectroscopic analysis of their 1200 nm emission band. We achieve *in vivo* intratumoral thermal sensing with temperature uncertainties well below 1 ^{o}C making possible the successful performance of fully controlled, highly efficient photothermal therapies of tumors in small animal models. Results included in this work do not only constitute a step towards minimally invasive photothermal therapies but also provide the community with a route towards the consideration of luminescent nanothermometry as a fully convincing technique for high sensitivity preclinical thermal sensing.

Introduction

Self-monitored photothermal agents (S-MPThs) are sort of nanoparticles (NPs) capable of efficient light-to-heat conversion and, simultaneously, of remote thermal sensing *via* luminescent thermometry.[1–5] This kind of NPs constitutes a unique platform for developing the minimally invasive, cost-effective and fully controlled hyperthermia therapies.[6–9] When dealing with the *in vivo* thermal treatment of tumors, S-MPThs make possible real time control over the intratumoral temperature that is required to drive it precisely into the therapeutic range.[10–13] This, in turn, allows the avoidance of both insufficient and overheating ranges, which could lead to either inefficient therapy or to excessive collateral damage, respectively.[14] As both heating and thermal readings are triggered by a single laser beam, such control could lead to simple and cost effective photothermal treatments. Several examples do exist in the literature demonstrating successful thermal *in vivo* treatment of tumors with S-MPThs, based on either lanthanide-doped NPs or infrared-emitting quantum dots (QDs). [15–20]

Recent works, however, have raised serious concerns about the reliability of sub-tissue thermal measurements based on luminescent nanothermometers and, therefore, also on S-MPThs.[21–24] It has been demonstrated how the non-homogeneous transmission of tissues can induce relevant spectral distortions and lead to erroneous thermal readouts that could be as large as 10 °C.[25–28] As such, previous results provided by S-MPThs in literature have been put in doubt. One of the most common pitfalls when dealing with intratumoral thermal reading is the fact that S-MPThs are surrounded by tumoral tissues and, therefore, the detected spectrum will always be modulated by its optical response.[29,30] Achieving artefact-free intratumoral thermal reading is not a trivial problem at all. At first glance, reliable thermal reading inside the tumor would require exact knowledge of the optical properties of the tumoral tissue in order to separate the tissue-induced spectral distortions from those purely caused by temperature variations. This assumption is not realistic due to the lack of knowledge of the optical properties of tumoral tissues and, particularly, of their temperature-dependence property. Alternatively, reliable intratumoral thermal reading could be achieved by using multiparametric S-MPThs.[31–35] These are a superior class of S-MPThs capable of providing multiple thermal readouts based on the analysis of different spectroscopic parameters such as intensity ratio, peak position, bandwidth, lifetime and/or emitted intensity.[19,28,36,37] Synchronised acquisition of multiple thermal reading unfolds a completely new way to check the accuracy of luminescent thermometry. The basic argument is the following: if the measurements are artefact-free, all the different thermal readings should converge. If the different thermal readouts diverge, however, it constitutes a clear indication that the luminescent nanothermometer is not working properly, namely that experimental artefacts are affecting crucially the measurements, in turn, distinctly affecting the luminescence feature of S-MPThs.

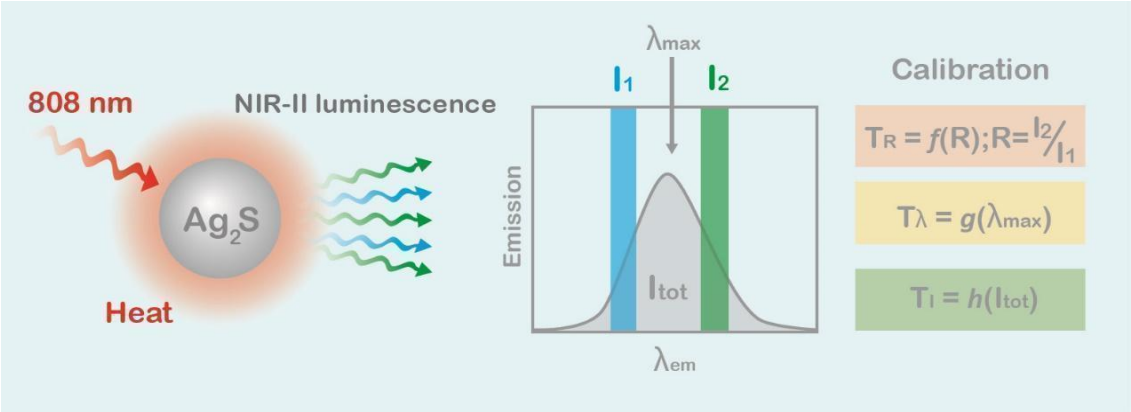

Figure 1.- Schematic representation of an Ag_2S nanoparticle operating as a self-monitored photothermal agent with capability for simultaneous multiple thermal readout, where T_R, T_λ and T_I represent the temperature readout given by three different parameters, which are intensity ratio, peak position and emitted intensity, respectively.

In this work, we introduce to the scientific community Ag_2S NPs as S-MPThs capable of simultaneous multiparametric thermal sensing (system schematically represented in **Figure 1**). Although the light-to-heat conversion efficiency and the multiparametric thermal sensing potential of Ag_2S NPs have been demonstrated separately, in this work we combine them both to achieve efficient *in vivo* photothermal treatment of tumoral tissues with a precisely real-time thermal control. The conditions that need to be satisfied and the analysis principles that must be followed are critically analysed. The implications that the procedure here proposed will have on the next steps of *in vivo* luminescence nanothermometry are also discussed.

Results and discussion.

Characterization of Ag_2S NPs as S-MPThs.

Ag_2S NPs used along this work were provided by Sinano Ltd (China). Details about the synthesis method as well as of their physical properties are provided in the **Supporting Information Section S1**. Firstly, the heating and multiparametric thermal sensing capacities of our Ag_2S NPs were systematically investigated. **Figure 2** summarizes the temperature dependence of the luminescence properties of our Ag_2S NPs. **Figure 2(a)** includes the emission spectra obtained from a water solution of Ag_2S NPs under 808 nm laser excitation, as obtained at different temperatures. Data included in **Figure 2(a)** reproduces previous results that revealed the presence of an intense thermal quenching accompanied by a red-shift of this emission band due to the temperature increment in the bandgap energy.[38,39] This simultaneous quenching and spectral shift provide possibility for single-shot multiparametric luminescence thermal reading. **Figure 2(b), (c) and (d)** show the thermal dependence of the emitted intensity ($I(T)$), peak position (λ_p(T)) and ratio between the emitted intensities at 1225 and 1175 nm ($R(T)$), respectively. As observed, the peak position and the intensity ratio presented close-to-linear increments with temperature, while the emitted intensity decreased in a non-linear behaviour. This, in turn, is in good agreement with the increment of the bandgap energy of Ag_2S NPs with temperature. The graphs in **Figure 2(b), (c**) and **(d)** also include the related relative thermal sensitivities obtained from the analysis of the different spectroscopic parameters:

Intensity: $S_r^I(T) = \frac{1}{I(T)}\frac{dI(T)}{dT}$ Eq.1

Peak position: $S_r^\lambda(T) = \frac{1}{\lambda_p(T)}\frac{d\lambda_p(T)}{dT}$ Eq. 2

Intensity Ratio: $S_r^R(T) = \frac{1}{R(T)}\frac{dR(T)}{dT}$ Eq. 3

The intensity-corresponding relative thermal sensitivities $S_r^I(T)$have been found to be strongly temperature-dependent being close to 5% at room temperature and decreasing down to 4.1% at 50 °C. The wavelength-based relative thermal sensitivity $S_r^\lambda(T)$ is virtually temperature-independent. Finally, the ratiometric thermal sensitivity $S_r^R(T)$, is also found to be temperature-dependent, decreasing from 1.4% at room temperature down to 1.0% at 50 °C. Data included in **Figure 2** do not only clearly certify the ability of Ag_2S NPs for multiparametric thermal sensing, but also reveal non-negligible temperature dependences in their thermal sensitivities. This fact, as it is shown later, has relevant experimental implications and forces temperature readouts to be obtained through an iterative process.

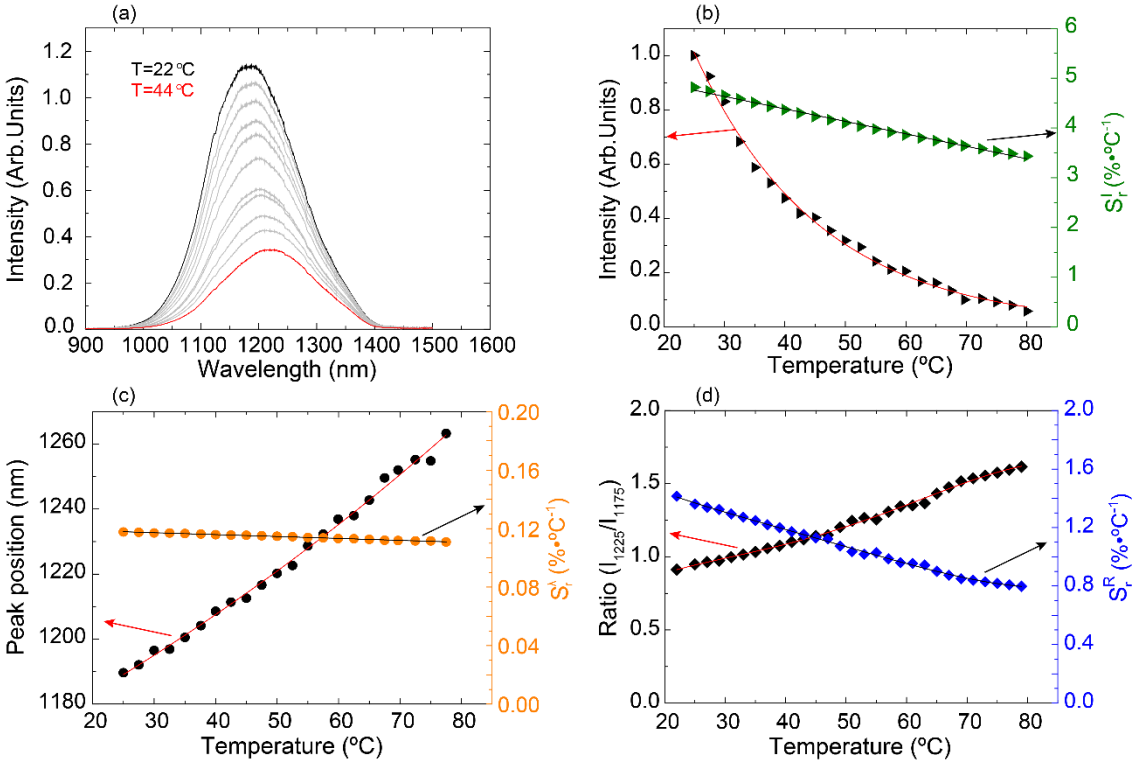

Figure 2.- (a) Emission spectra of an aqueous suspension of Ag_2S NPs as obtained at different temperatures. The temperature induced quenching and spectral shift is evidenced. **(b)** Temperature dependence of the emission intensity (black dots) generated by Ag_2S NPs and the relative thermal sensitivity (green dots) at different temperatures. **(c)** Temperature dependence of the peak position (black dots) of the Ag_2S NPs emission band and the temperature-induced relative thermal sensitivity variation (orange dots) included. **(d)** Temperature dependence of the ratio (black dots) between the emitted intensities at 1175 nm and 1225 nm as well as the ratiometric relative thermal sensitivity (blue dots). In all the graphs, dots are the experimental data, while the line is a guide for the eyes. The temperatures were obtained by a thermal camera after the heating process of sample.

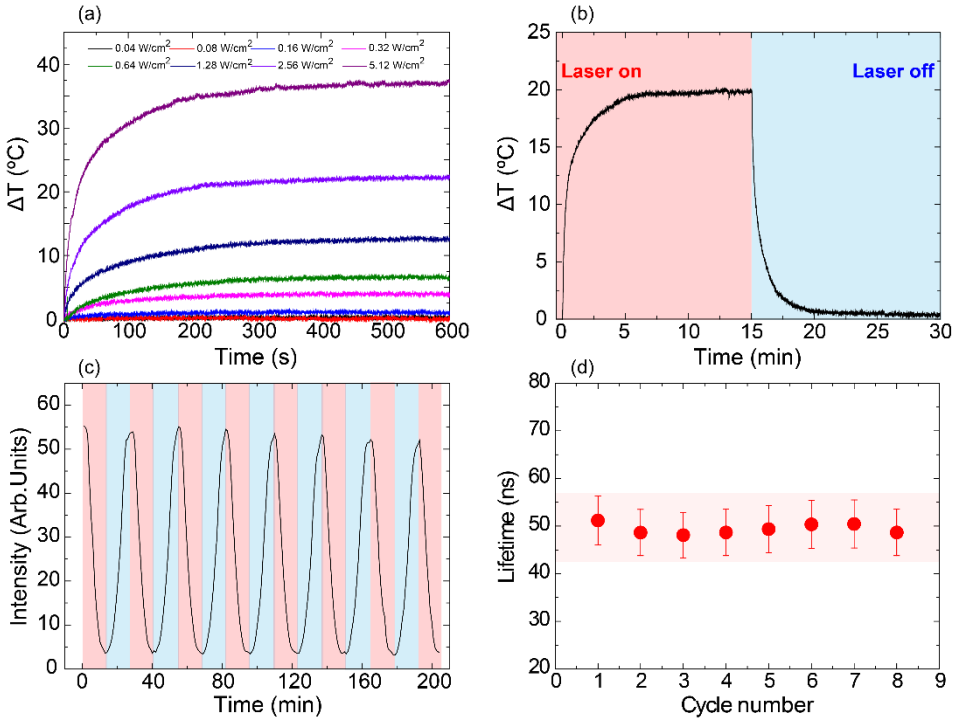

Figure 3.- (a) Time evolution of the temperature of an aqueous solution of Ag_2S NPs optically excited by an 808 nm laser as obtained different power densities. **(b)** Time-evolution temperature increment of an aqueous solution Ag_2S NPs excited by 808 nm laser (a power at 505 mW). The laser was kept on for 15 min (red part) until the solution temperature reached a stable value then turned it off until the temperature relaxed to surrounding temperature (blue part). **(c)** Temperature driven change of the emitted intensity generated by an aqueous solution of Ag_2S NPs subjected to repetitive heating (red)-cooling (blue) cycles during 200 min. **(d)** Fluorescence lifetime of Ag_2S NPs dispersed in water after consecutive cooling cycles. The maximum and minimum temperatures of the thermal cycles in **(c)** and **(d)** are 55 ºC and 22 ºC, respectively.

Once the thermal-sensing multifunctionality of Ag_2S NPs was demonstrated, their capability to operate as photothermal agents was evaluated. A colloidal suspension of Ag_2S NPs was illuminated with an 808 nm laser at different power densities and its temperature was dynamically recorded by a thermal camera. The results are included in **Figure 3(a)**. Relevant heating is observed for laser power densities typically used for *in vivo* tumor photothermal therapies (1 W/cm^2), revealing that the Ag_2S NPs possess a non-negligible laser-to-heat conversion efficiency. The steady state temperature has been found to be proportional to the laser power density (see **Supporting Information Section S2**). This, in turn, suggested the lack of saturation effects and damage of the Ag_2S NPs even with temperature increments over 30 °C. The efficient light-to-heat conversion should obey to the presence of large nonradiative decay rates from the conduction to the valence band of Ag_2S NPs. This fact has been confirmed by Quantum Yield (QY) measurements performed following the experimental procedure described in **Experimental Section**. The QY is here defined as the number of emitted photons divided by the number of absorbed photons and can be written as:

$$QY = \frac{n\,º emitted\ photons}{nº\ absorbed\ photons} = \frac{W_{rad}}{W_{rad}+W_{nonrad}} \qquad \text{Eq. 4}$$

where W_{rad} and W_{nonrad} are the radiative and nonradiative decay rates of Ag_2S NPs, respectively. At 27 °C, the QY of Ag_2S NPs in the water is as low as 0.08 % (see details in **Supporting Information Section S3**). This means that nonradiative decay rates in Ag_2S NPs are

orders of magnitude larger than the radiative decay rates, in turns, predicted the Ag_2S NPs possess a high heating efficiency which determined by the nonradiative decay rates. The heating efficiency of a Ag_2S NP (η_h) system is defined as the fraction of the absorbed energy that it is released in the form of heat:

$$\eta_h = \frac{heat\ released}{absorbed\ energy} = 1 - QY\frac{\lambda_p}{\lambda_f} \qquad \text{Eq. 5}$$

where $\lambda_p = 808$ nm and $\lambda_f = 1200$ nm are the pump and averaged fluorescence wavelengths, respectively (see **Supporting Information Section S4** for more details on how **Eq. 5** is deduced). At 27 °C, for a QY of $8{\cdot}10^{-4}$, the heating efficiency of Ag_2S NPs has been estimated to be over 99.9%. This means that when an Ag_2S nanoparticle is optically excited by an 808 nm laser, nearly all the absorbed power is virtually converted into heat. The heating efficiency of Ag_2S NPs has been experimentally determined by following the method reported by Roper *et al.*[40] **Figure 3(b),** shows the time evolution of the temperature of a colloidal solution of Ag_2S NPs when subjected to a laser-induced heating and a subsequent free-cooling event. Calculations made on the experimental data included in **Figure 3(b)** leads to a heating efficiency close to 93.2% (see more details in **Experimental Sections**). This value is somehow lower than the one derived from the estimation of QY but, indeed, reveals a heating efficiency close to 100%. The discrepancies can be attributed either to an underestimation of the QY and/or to the presence of artefacts during the experimental determination of η_h such as unknown sample-medium heat transfer rate or pump beam depletion due to large absorption coefficients.

In order to check the thermal stability of Ag_2S NPs, we subjected them to consecutive heating and cooling cycles. The fluorescence intensity during these cycles was continuously monitored. Results are shown in **Figure 3(c)**, where red and blue areas indicate heating and cooling, respectively. As it can be observed, the luminescence intensity significantly decreases during heating due to the thermal quenching already discussed. More importantly, the luminescence intensity is completely recovered after the cooling process. This indicates the absence of any relevant damage of Ag_2S NPs caused by accumulative heating. The minimum deterioration in the luminescent properties of Ag_2S NPs subjected to consecutive heating cycles was further evidenced by lifetime measurements performed after each heating and cooling cycle. Results are included in **Figure 3(d)**. Fluorescence lifetime of Ag_2S NPs remained almost unperturbed by the heating/cooling procedure. This again reveals the negligible creation of defects (luminescence quenchers). In summary, data included in **Figure 3** reveals that Ag_2S NPs are efficient and robust photothermal agents.

Figure 2 and **3** demonstrate that Ag_2S NPs account for a unique combination of thermal sensing and heating capacities that make them ideal candidates for fully controlled *in vivo* photothermal therapies. The thermal sensing and heating properties of Ag_2S NPs are listed in **Table 1** together with those previously determined for other photothermal agents successfully used for *in vivo* therapy. It is worth noting that Ag_2S NPs are the unique system capable of efficient light-to-heat conversion while making possible multiparametric thermal sensing *via* infrared luminesce thermometry. In addition, Ag_2S NPs show the largest thermal sensitivities and the best light-to-heat conversion efficiency among their counterparts.

Table 1 Properties comparisons of different thermal therapy agents

System	Thermal feedback	S_r (% °C^{-1})	Multi-sensing	η_h(%)	σ_{abs}@ 800 nm (cm^2)	Ref.
$NdVO_4$	NO	2.67	NO	72.1	2.5×10^{-20}	(18)
SWCNTs	NO	0.005	NO	3.6	1×10^{-17}	(41–45)
$Au@Gd_2O_3$	NO	1.24	NO	55.7	4.3×10^{-11}	(46)
Au nanorods	NO	1.16	NO	50	2.3×10^{-15}	(47–49)
Polypyrrole	NO	0.19	NO	44.7	8.5×10^{-12}	(50,51)
CdTe	NO	0.08	YES	14	5.83×10^{-24}	(52,53)
MWCNTs	NO	0.12	NO	16.6	9.8×10^{-22}	(54–56)
Carbon nanodots	YES	1.79	NO	30.6	2.09×10^{-23}	(57–59)
$NaYF_4$:Yb,Er@$NaYF_4$:Yb@ PDA-ICG	YES	1.11	NO	15.9	9.11×10^{-21}	(60,61)
LaF_3: Nd	YES	0.2	YES	12.5	5.44×10^{-20}	(62,63)
Ag_2S	**YES**	**4**	**YES**	**93.2**	**3.46×10^{-22}**	**This work**

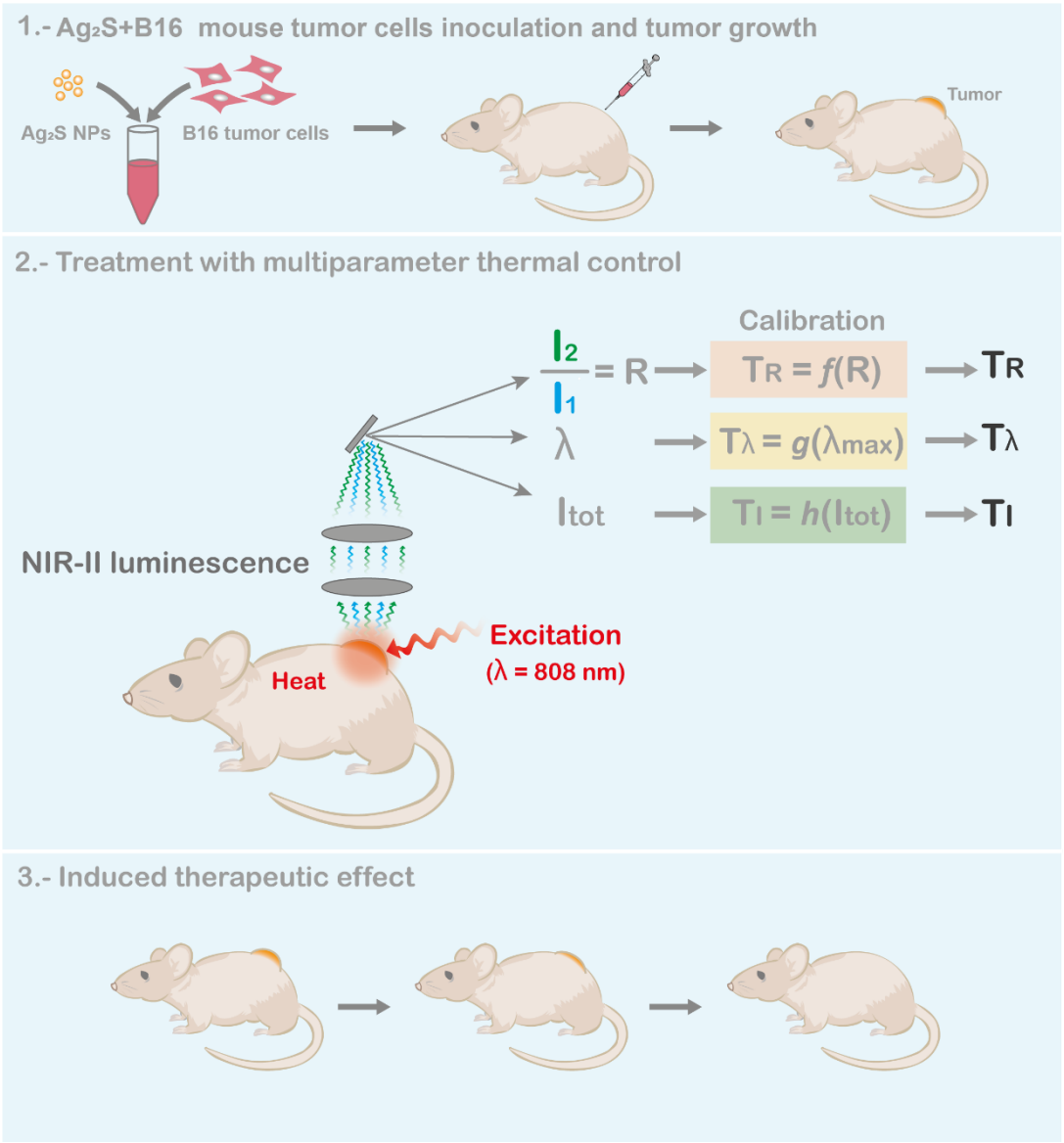

Figure 4.-Schematic representation of the in *vivo* photothermal treatment of tumors developed in this work. The Ag_2S NPs are used as dual agents capable of laser-induced heating and multiparameter and accurate intratumoral thermal reading during treatment.

In Vivo photothermal treatment of cancer tumor with precise thermal feedback.

The experimental procedure adopted to demonstrate the potential of Ag_2S NPs for multiparametric *in vivo* intratumoral thermal sensing is schematically drawn in **Figure 4**. For *in vivo* experiments, we employed C57BL/6 mice. This particular strain was selected due to its strong (black) pigmentation so that the performance of Ag_2S NPs would be tested in the presence of a highly absorbing tissue also providing a strong autofluorescence background. [64] In other words, we here evaluate the potential use of Ag_2S NPs under the most adverse circumstances. This is at odds with previous works dealing with nanoparticle-assisted photothermal treatments in which either white or nude mice were used. [65] The use of pigmentation-free strains (white mice or nude mice) allows photothermal treatment easier due to the larger transmission of tissues they have and, also, the short of autofluorescence can reduce the interference to luminescence signal of NPs. Moreover, the light-colour tissues would lack parasite laser which avoids inducing tissues heating. Tumor inoculation was performed by a subcutaneous injection of 150 µL of a solution containing 75 µL of cells (around 10^6 cells/ml)

and 75 µL of Ag_2S NPs solution (1.5 mg/mL in PBS). Simultaneous injection of cancer cells and thermal agents avoids the requirement of an intratumoral injection (a procedure followed in previous works [66]) that typically leads to the gathering of S-MPTh at the tumor's surface due to leakage of injected solution through the injection path. The presence of even a small fraction of thermal reporters at the tumor surface avoids reliable intratumoral thermal reading (they provide information about the temperature at the surface instead of within the tumor). Five days after inoculation, an incipient tumor appeared. Then, it was subjected to a 4-min-long photothermal treatment by illuminating the tumor with an 808 nm laser beam. NIR-II fluorescence images reveal that Ag_2S NPs remained at tumor location during, at least, five days after inoculation (see **Supporting Information Section S5**). At this point it is not possible to clarify whether the Ag_2S NPs are incorporated inside cancer cells or they are just imbedded within the tumoral tissue. But the fluorescence images including in **Figure S4** reveal that the Ag_2S NPs are co-localized with the tumor so that their thermal readout would correspond to the intratumoral temperature. The emission generated by the Ag_2S NPs within the tumor was registered by a multimode fibre placed in proximity to the tumor. The fibre was coupled to a NIR-II spectrometer that allowed spectrum acquisition every 1 second. More details about the experimental set-up can be found in **Supporting Information Section S6**.

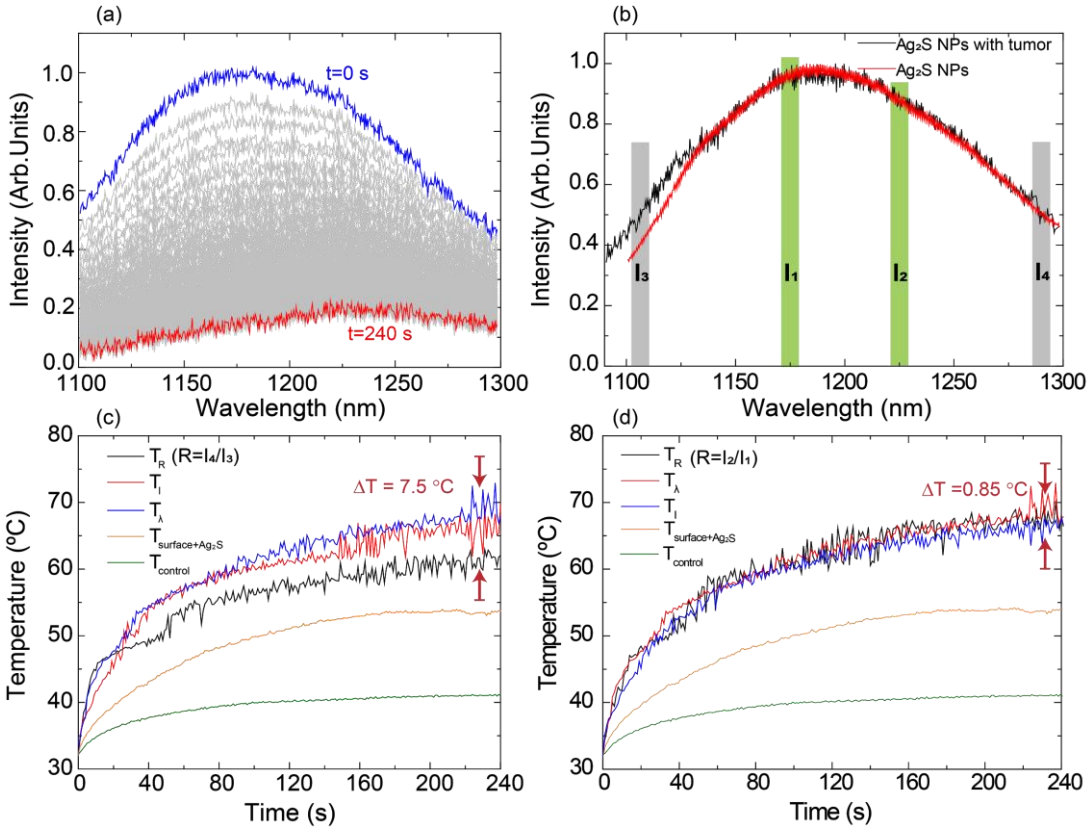

Figure 5.- **(a)** Time-evolution emission spectra of intratumoral Ag_2S NPs during photothermal treatment. **(b)** Comparison of the room temperature emission spectra of Ag_2S NPs as obtained when they are in an aqueous suspension and within the tumor. The spectra comparisons at higher temperatures are included in **Support Information Section S7**.The tissue-induced spectral distortions for wavelengths below 1125 nm are evident. Shadow regions indicate the different wavelengths used for ratiometric thermal sensing. **(c)-(d)** Time evolution of laser-induced tumor temperature increment during photothermal treatment as calculated from the analysis of the peak position (T_λ), emitted intensity (T_I), and intensity ratio (T_R). In **(c)** and **(d)**, T_R was calculated based on the different intensity ratio I_4/I_3 and I_2/I_1, respectively. The reason

why these four particular wavelengths were chosen will be addressed later. The control experiment is also included by displaying the time evolution of laser-induced tumor heating in absence of Ag_2S NPs.

Figure 5(a) shows the emission spectra generated by Ag_2S NPs within a tumor being treated with a 1 W/cm^2 power density as obtained for different time treatments (t = 0 s corresponds to the treatment beginning and t = 240 s correspond to the end of treatment). Simultaneous intensity reduction and red-shift of the emission band is observed during the treatment, pointing out intratumoral thermal heating during treatment (see **Figure 2**). The analysis of the intratumoral emission can be used to get the time evolution of intratumoral temperature. But, as pointed in the introduction, recent works revealed that prior to extract thermal information from the emission spectra it is mandatory to evaluate at which extent the registered spectra are distorted by tissue extinction. For the sake of comparison, **Figure 5(b)** shows the emission spectrum at room temperature as obtained for Ag_2S NPs inside the tumor before treatment together with the emission spectrum corresponding to Ag_2S NPs in an aqueous solution obtained under exactly the same experimental conditions. Both emission spectra are quite similar in the 1125-1300 nm wavelength range, even though noticeable differences were observed for wavelengths shorter than 1125 nm. These differences are attributed to the tissue-induced spectral distortions caused by the particular attenuation (light scattering and absorption) of tumoral tissues for wavelengths shorter than 1125 nm. Note that this is a first order assumption, its corroboration would require the detailed knowledge of the optical properties of the tumoral tissue, a topic that is out of the scope of this paper. Data included in **Figure 5(b)** reveals that, for these particular measurements, the acquisition of reliable intratumoral thermal readouts would only be possible from the analysis of intratumoral emission spectra in the 1125-1300 nm spectral range. The spectral properties out of this range would be contaminated by the tissue-induced spectral dispersions and, consequently, would lead to erroneous thermal readouts.

The thermal readout obtained from the emission spectra included in **Figure 5(b)** depends critically on the analysis procedure and criteria. In order to illustrate this fact, intratumoral temperature has been calculated following two different protocols. The first one replicates the simple procedure used up to now (hereafter “traditional procedure”) and is based on the analysis of emission spectra without considering the possible presence of tissue-induced spectral distortions. When following such a protocol, the tissue temperature increments calculated from the analysis of the variation of emission intensity (I), wavelength shift (λ)and ratio (R) were given by:

$$\Delta T^{I}_{std}(t) = \int_{I^{std}(t=0)}^{I^{std}(t)} \frac{1}{S_r^{I^{std}}} \frac{\left|dI^{std}\right|}{I^{std}} \tag{3}$$

$$\Delta T^{\lambda}_{std}(t) = \int_{\lambda(t=0)}^{\lambda(t)} \frac{1}{S_r^{\lambda}} \frac{|d\lambda|}{\lambda} \tag{4}$$

$$\Delta T^{R}_{std}(t) = \int_{R^{std}(t=0)}^{R^{std}(t)} \frac{1}{S_r^{R^{std}}} \frac{\left|dR^{std}\right|}{R^{std}} \tag{5}$$

where I^{std} was obtained by integrating the whole emission spectrum from 1100 to 1300 nm and R^{std} was the intensity ratios obtained by dividing the intensities generated at 1110±5 and 1280±5 nm ranges (denoted as I_3 and I_4 in **Figure 5(b)**). These particular wavelengths (1110 nm and 1280 nm) were chosen due to the fact that (as it has been traditionally thought), when dealing with ratiometric thermal measurements, the larger the difference between evaluated wavelengths, the better the readout would be.[67] $I^{std}(t=0)$, $R^{std}(t=0)$ and $\lambda(t=0)$, in turn, were the intensity, ratio and peak position at the beginning of the heating cycle, respectively (which correspond to the ones at 32 °C, *i.e.* the initial intratumoral temperature). The integrals in (3)-(5) were all calculated after expressing the relative thermal sensitivity as a direct function of the corresponding thermometric parameter (instead of temperature). The time evolution of the multiparametric thermal readouts calculated by following the "traditional" procedure are included in **Figure 5(c)**. The temperature evolution of a tumor, in the absence of any Ag_2S NPs, subjected to the same illumination procedure, is also included (denoted as "control"). In this case, only the tumor's surface temperature was accessed (with a thermal camera). It is clear that the comparison among the thermal readings based on the different parameters shows that the presence of Ag_2S NPs within the tumor leads to a relevant laser-induced heating, whatever the spectral parameter used for thermal reading. This is a consequence of the high light-to-heat conversion efficiency of Ag_2S NPs that dominates over the intrinsic tissue heating. **Figure 5(c)** also includes the time evolution of the surface temperature of a tumor with Ag_2S NPs as registered by an infrared thermal camera. It is evident that the tumor surface temperature is significantly lower than the intratumoral temperature provided by Ag_2S NPs. This is in accordance with previous works and agrees with the fact that heating source (Ag_2S NPs) are located inside the tumor. **Figure 5(c)** disclose discrepancies in excess of 7°C between the thermal readouts obtained from the analysis of the different spectral parameters. Such a large thermal divergence reduces the reliability of the thermal measurements as it is difficult to elucidate *a priori* which of the spectral parameters is providing the correct intratumoral temperature. In addition, such uncertainty is not acceptable when dealing with thermal measurements in biological systems. After all, a tiny change in only a few degrees can have a great impact for the whole system. We must note that, at this point, the lack of reliability of the "traditional" procedure was not directly evidenced in previous works, as this is the first time that multiparametric thermal analysis is performed *in vivo*.

In order to improve the reliability and robustness of the thermal measurements, the presence of tissue-induced spectral distortions should be avoided. For this, it is mandatory to identify those spectral regions where the tissue-induced spectral distortions could be considered as negligible. The most straightforward steps to do this are: (i) estimate the initial temperature of the system by a second method (such as a thermographic camera), (ii) take the initial luminescence spectrum obtained under *in vivo* conditions and (iii) compare it with the calibration spectrum (obtained without any tissue) corresponding to that initial temperature. Such a comparison can be done after normalizing the data to the area under the curve in that range, as done in **Figure 5(b)**. The comparisons reveal that the non-affected spectral range goes from 1140 nm to 1300 nm. This, in turn, means that the transmission of this particular tumoral tissue is approximately flat in this wavelength range. The temperature variations are now estimated as:

$$\Delta T^I(t) = \int_{I(t=0)}^{I(t)} \frac{1}{S_r^I} \frac{|dI|}{I}$$

(6)

$$\Delta T^{\lambda}(t) = \int_{\lambda(t=0)}^{\lambda(t)} \frac{1}{S_r^{\lambda}} \frac{|d\lambda|}{\lambda} = \Delta T_{std}^{\lambda}(t)$$

(7)

$$\Delta T^{R}(t) = \int_{R(t=0)}^{R(t)} \frac{1}{S_r^{R}} \frac{|dR|}{R}$$

(8)

where I was obtained by integrating the whole emission spectrum from 1140 to 1300 nm and R was the intensity ratio obtained by dividing the intensities generated at 1175±5 and 1225±5 nm ranges (denoted as I_1 and I_2 in **Figure 5(b)**). The analysis of the peak position remained the same because, according to the experimental data, the tissue-induced distortion does not affect the spectral position of the emission peak. The time course of intratumoral temperature obtained by applying expressions (6)-(8) to the experimental data of **Figure 5(a)** are included in **Figure 5(d)**. It is worth to note, the analysis from the intensity, peak position or intensity ratio provide results that are virtually identical. Actually, the thermal discrepancies among the different readings of the intratumoral temperature are well below 1 °C. This is a hardly disputable indicator of the correctness of the thermal readouts. As discussed in **Section S8 of Supporting Information**, this could only mean one of two things: (i) either the thermometric parameters were selected so that the thermal dependence of the optical properties of the tissue were completely avoided or (ii) the tissue-induced effects have the exact same contribution on the estimations of temperature by different thermometric parameters. While the latter would imply an improvement in preciseness only, the former would entail an enhancement in accuracy as well. The question concerning which of these two conditions is factual can only be answered by a thorough consideration of the thermal dependence of scattering and absorption of light in several biological tissues. Such a study, however, is out of the scope of this work. Nevertheless, whichever case is true, the reliability of the thermal readout is improved when compared with the "traditional" procedure. For this reason, we here propose the second approach as a safety step for the analysis of future *in vivo* luminescence thermometry studies. At this point, it is worth emphasizing that, due to stronger attenuation-induced effects, tumors that are more internalized than melanoma might request more elaborated protocols for the analysis of the data.

Previous works have demonstrated that valuable information about the properties of a given tissue can be obtained from the analysis of its heating or cooling thermal curves.[72] Transient thermometry has been, indeed, used to determine thermal properties of tissues, to detect in advance tumor development or even to diagnosis ischemic tissues.[73-75] In the simplest of the approaches the temperature should follow an exponential trend with a characteristic time (τ) that depends on the thermal and physical properties of the tissue under study (see **Supporting Information S9**). The analysis of the intratumoral heating curves included in **Figure 5(d)** reveal that in our experimental conditions (tumor being subjected to a heating in excess of 30 ºC) the heating curve does not follow an exponential trend (see **Supporting Information Section S9**). We state at this point that this discrepancy is a clear indicator that the physical properties (including thermal, absorption and scattering properties) are changing during the treatment, thus leading to a time dependent thermal characteristic time τ. This is in accordance with the

results included in the next section that demonstrates the complete tumor eradication due to the photothermal treatment.

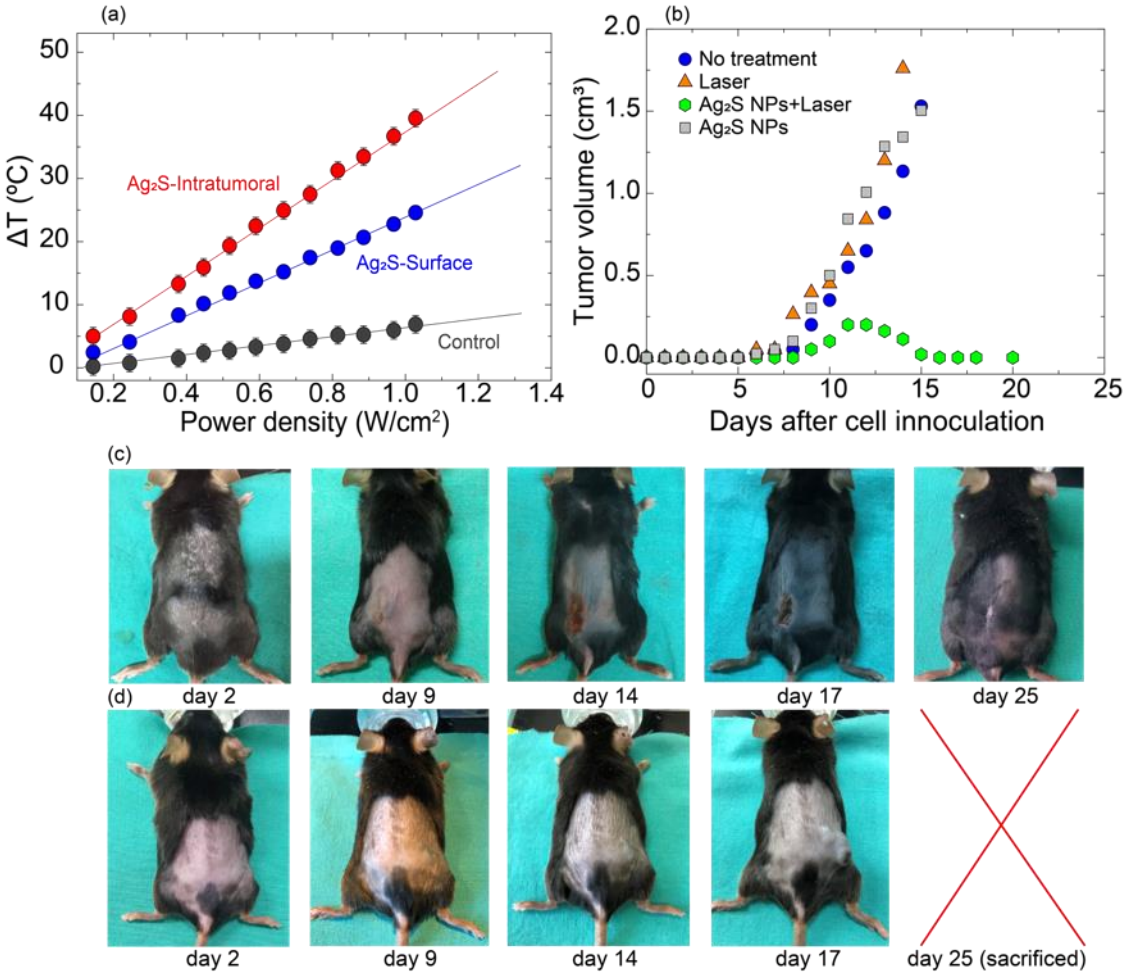

Figure 6.- (a) Intratumoral and surface temperature increment as a function of the 808 nm laser power density as obtained for a tumor injected with Ag_2S NPs acting as heating and thermal sensing agents. Data obtained for a control tumor (without Ag_2S NPs) have also been included. **(b)** Time evolution of tumor volume after different photothermal treatments. **(c)-(d)** Optical pictures of mice after tumor + Ag_2S NPs inoculation. Optical photos in **(c)** correspond to a mouse subjected to a photothermal treatment (808 nm irradiation at 1 W/cm^2) whereas **(d)** corresponds to a control mouse not subjected to any treatment.

In Vivo tumor ablation by Ag_2S NPs.

Once the correct procedure was found to accurately estimate the intratumoral temperature, it was possible to elucidate the intratumoral heating as a function of the 808 nm laser irradiation density due to the light-to-heat conversion of Ag_2S NPs. For the sake of comparison, the surface temperature of the tumor was also simultaneously recorded with a thermal camera. Results are included in **Figure 6(a).** Both the intratumoral and tumor surface temperatures have been found to linearly increase with the laser irradiation density within the 0.1-1.1 W/cm^2 range. For all the laser power densities, the intratumoral temperature was found to be larger than the surface´s temperature, due to the intratumoral location of the Ag_2S nanoheaters as discussed above. Experiments were also performed on tumors without Ag_2S NPs. In this case, due to the absence of Ag_2S NPs, the tumoral heating was only evaluated by a thermal camera. The surface temperature of these "control" tumors as obtained for different 808 nm laser power densities are also included in **Figure 6(a)**. In this case, heating is only produced by the absorption of 808

nm laser radiation by the tissue. Its highest observed value (for 1.1 W/cm^2 laser density), however, was found to be well-below 10 ^{o}C. **Figures 5(d) and 6(a)**, therefore, reveal how Ag_2S NPs enables intratumoral thermal increments as large as 40 ^{o}C in a short time and by using moderate (<1 W/cm^2) laser power densities. According to previous works, this "fast and severe" heating produces irreversible damage on tumoral cells (causing what is typically referred as "tumor ablation").[68,69] This, in turn, results in a total treatment that does not require any complementary technique (such as chemotherapy, for instance).[70]

In order to evaluate the efficacy and selectivity of Ag_2S NPs as photothermal therapeutic agents, we systematically investigated the tumor evolution after photothermal treatment under four different situations: i) a tumor inoculated with Ag_2S NPs and not exposed to any photothermal treatment (Ag_2S+Tumor), ii) a tumor inoculated with Ag_2S NPs and subjected to a 4-min photothermal treatment with 1 W/cm^2 (Ag_2S+Tumor+Laser), iii) a tumor subjected to a 4-min photothermal treatment with 1 W/cm^2 (Tumor+Laser), and iv) a tumor not exposed to any photothermal treatment (Tumor). In all cases, the photothermal treatment was performed 5 days after inoculation. Tumor development was monitored through the time evolution of its volume. Results are included in **Figure 6(b)**. Only the tumor inoculated with Ag_2S NPs and subjected to laser irradiation shows an evolution that differs from the natural trend. Note that the time evolutions of tumor volumes obtained in the cases i), iii) and iv) are virtually identical. This fact evidenced that the Ag_2S NPs by themselves have no decremental effect on the behaviour of tumoral tissues and that, in their absence, the laser irradiation densities used in this work do not have any therapeutic effect. Note that the time course of tumor´s volume obtained for the successful case (Ag_2S+Tumor+Laser) reveals a complete tumor therapy. In fact, 10 days after treatment (15 days after inoculation) the tumor was completely removed. In the unsuccessful cases, the tumor´s volume was found to be close to 1.5 mm^3 on the 15th day after inoculation. This, in turn, made the sacrifice of the mice necessary. Complete tumor removal was evidenced in the optical pictures acquired at different days after inoculation as obtained for the "Ag_2S+Tumor+Laser" (**Figure 6 (c)**) and "Tumor" (**Figure 6(d)**) cases (the optical photos of another two cases"Ag_2S+Tumor" and "Tumor+laser" are offered in **Supporting Information Section S10**) . As observed, the photothermal treatment leads to a complete tumor removal that resulted in a longer survival. The nontreated mice had to be sacrificed at day 15 after inoculation whereas fully treated mouse survived more than 25 days after tumor inoculation without showing any evidence of tumor reappearance.

Conclusions

In summary, the possibility of having multiple readouts in a simultaneous way by means of different thermometric parameters was explored and demonstrated with Ag_2S NPs. These properties were combined with their over 90% light-to-heat conversion efficiency to provide a controlled photothermal therapy of tumor in small animal models. The convergence between the different estimations of temperature variation (with uncertainties well below 1 ^{o}C) in a heating transient was verified and proposed as a convincing indicator of the improved reliability of these luminescent thermometers. Results included in this work do not only constitute a step towards minimally invasive photothermal therapies, but also provides the community with a route to avoid artefacts produced by biological tissues. Though future studies might be necessary to completely account for the tissue-induced effects, this work certainly contributes to the consideration of luminescent nanothermometry as a convincing technique for high sensitivity preclinical thermal sensing.

Experimental section

Ag_2S NPs: Ag_2S-PEG NPs dispersed in water were purchased from SINANO Int. (China).

Physical characterization: X-ray diffraction pattern was recorded by a Philips X'pert diffractometer with Cu-Kα radiation at 45 kV and 40 mA. The data were collected from 2θ = 20°-90° with a step size of 0.02° and a normalized count time of 1 s/step**.** Transmission electron microscopy (TEM) image was obtained by using a transparent electron microscope (TEM, TECNAI G2, the resolution is 0.2 nm) with an acceleration voltage of 200 kV

Spectroscopic characterizations: The emission spectra were achieved by using an InGaAs CCD camera (Andor iDus DU490A) then the acquired luminesce signals were analysed by an Andor Shamrock 193i spectrometer, while the aqueous suspension of Ag_2S NPs in the quartz cuvette was excited by the 808 nm LIMO laser diode (Lumics). Additionally, the spectrometer was equipped by the heating plate (heidolph, MX07R-20-HD2E) to study the temperature effect to the Ag_2S NPs emission. Time-evolution emission spectra of intratumoral Ag_2S NPs were acquired by the Andor Shamrock 193i spectrometer with Kinetic mode. The luminescence decay curves were recorded by exciting the aqueous suspension of Ag_2S NPs by using an Optical Parametric Oscillator (Quanta Ray, OPO) laser equipped with the heating plate (Linkam, T96-PE) to tune the temperature. The OPO laser provides 10 ns pulses with an average energy of 0.2 J and a frequency of 10 Hz.

Quantum yield measurement of Ag_2S NPs: The absolute quantum yield (QY) was measured with a calibrated spectrofluorometer (Edinburgh Instruments, FLS920) equipped with an integrating sphere (Jobin-Yvon), while Ag_2S NPs were put into a cuvette then excited with a Xe lamp which filtered with a long-pass filter (610 LP, Thorlab Inc.) and a monochromator (wavelength at 800 nm, and bandwidth is 20 nm). Moreover, the detector was equipped with a NIR photomultiplier tube (Hamamatsu, R5509-72) which is always kept cooling in the liquid-nitrogen atmosphere. Then the QY value is obtained through dividing the total number of emitted photons in the 900-1700 nm wavelength range by the total number of absorbed photons at 800 nm, as described in the Eq. (1).

Estimation of Ag2S NPs heating capability under different power densities: 300 μL aqueous solution of Ag_2S NPs (1.5 mg/mL) was put into an open quartz cuvette then excited with 808 nm laser (Lumics) under different power densities while the temperature change was monitored by a NIR thermal camera (FLR 40bX).

Photothermal conversion efficiency calculation of Ag_2S NPs through experimental data: The photothermal conversion efficiency (η_h) is a value to estimate the heating conversion ability of nanoparticles, namely the proportion of absorbed laser energy that is transformed into heat. The method of calculation followed here is reported by Roper *et. al.* [40] and the details are listed below:

The aqueous solution of Ag_2S NPs (1.5 mg/mL) was put into an open quartz cuvette then excited with 808 nm laser (Lumics, at a power of 505 mW) while monitoring the temperature change by a NIR thermal camera (FLR 40bX). When the temperature of suspension reached a stable value

(here it took 15 min), straight after turning off the laser to wait for the temperature relaxation until equal to the surrounding environment temparatute.

The formula for calculating η_h can be defined as:

$$\eta_h = \frac{hA(T_{max}-T_0)-Q_0}{P\left(1-10^{-OD}\right)} \quad (1)$$

where *h* is the heating transfer coefficient, *A* is the surface area of the quartz cuvette where the solution is placed. T_{max} and T_o are the stable temperature reached by the solution after continuous laser excitation for 15 min and the temperature of the surrounding environment, respectively. Q_0 represents the heat dissipated from the laser absorbed by solvent container, while *P* is the laser power and *OD* is the optical density of the solution sample.

According to the results reported by Roper et. al., the value of *hA* could be obtained through temperature relaxation time τ (determined from the cooling process shown in Figure 3 (b)), which could be defined as:

$$hA = \frac{mC_p}{\tau} \quad (2)$$

where m = 0.3 g and C_p = 4.184 $J \cdot g^{-1} \cdot ℃^{-1}$ represent the mass and heating capacity of the solvent (water in our work) respectively. Then substitute the value of *m* and *Cp* into the formula (2) as well as the obtained τ = 65.17 s, then the value of *hA* is equal to 19.33 $mW \cdot ℃^{-1}$.

The temperature increment could be obtained from the heating-cooling curve (**Figure 3(b)**), which is 19.9 ℃. Additionally, the laser power *P* is 505 mW and the optical density (*OD*) is 0.50 at this concentration under 808 nm laser. And Q_0 was estimated as 63 mW through measuring the laser power lost after passing through the opening quartz cuvette filled with the same volume of distilled water. Substituting all these values into the formula (1), then obtained the photothermal conversion efficiency of the aqueous solution of Ag_2S NPs is 93.2%.

Cell culture and animal studies.

***Cell culture*:** The murine melanoma B16 is a spontaneously arising melanoma of C57BL/6 mice, from which the B16 cell line was established. We have used this commercially available cell line (ATCC® CRL-6322™, Manassas, VA, USA) for the *in vivo* experiments. Cells were plated onto sterile T75 flasks (Thermo Fisher Scientific, Waltham, MA USA) and cultured with DMEM medium (Thermo Fisher Scientific), supplemented with 10% foetal bovine serum and antibiotics (100 U/ml penicillin, 100 µg/ml streptomycin, all from Thermo Fisher Scientific), in a humidified incubator with 5% CO_2. After reaching 75-80% confluence, cells were trypsinized and centrifuged at 1000 g for 5 minutes. Cells were resuspended in 200 µL of sterile PBS and counted using a Neubauer chamber.

***Animal studies*:** All the experiments were conducted in accordance with the European Union directives 63/2010UE and Spanish regulation RD 53/2013. Animal Ethics Committee of the Universidad Autónoma de Madrid also approved the use of these animals. We used 6 to 12-week-old female C57BL/6 mice to induce melanoma, a well-established and widely used tumor

model. [71] Briefly, mice were anesthetized with isoflurane in 100% oxygen, placed in the prone position on the operating table and hair was removed with an electric shaver and hair removal cream to leave the back of the animal exposed for injection. With a 1-ml syringe with attached 27½-G needle, we inserted the needle superficially, so that it was visible through the skin. A subcutaneous injection of 150 µL containing a dose of 1×10^5 B16 cells (which is 1.5 to 2 times the minimal tumorigenic dose in normal C57BL/6 mice) and 75 µL of Ag_2S-PEG NPs dispersed in PBS (1.5 mg/mL). The application resulted in a clear "bleb". A palpable tumor appeared as soon as 4-5 days and was observed until it grew to an approximate size of $1 \times 1 \times 1$ cm^3 in around 17 days. At this point, the tumors became necrotic in the top and began to ulcerate or bleed; and we ethically sacrificed the mice.

References

[1] X. H. Wang, X. Q. Chen, H. S. Peng, X. F. Wei, X. J. Wang, K. Cheng, Y. A. Liu, W. Yang, *J. Mater. Chem. B* **2020**, *8*, 1033.

[2] Z. Y. Zhang, H. Suo, X. Q. Zhao, C. F. Guo, *Photon. Res.,* **2020**, *8*, 32.

[3] S. Yakunin, B. M. Benin, Y. Shynkarenko, O. Nazarenko, M. I. Bodnarchuk, D. N. Dirin, C. Hofer, S. Cattaneo, M. V. Kovalenko, *Nat. Mater.* **2019**, *18*, 846.

[4] C. D. S. Brites, S. Balabhadra, L. D. Carlos, *Adv. Opt. Mater.* **2019**, *7*, 1801239.

[5] F. Vetrone, R. Naccache, A. Zamarrón, A. Juarranz de la Fuente, F. Sanz-Rodríguez, L. M. Maestro, E. M. Rodriguez, D. Jaque, J. G. Solé, J. A. Capobianco, *ACS Nano* **2010**, *4*, 3254.

[6] G. L. Ni, G. Yang, Y. He, X. L. Li, T. Y. Du, L. Xu, S. B. Zhou, *Chem. Eng. J.* **2020**, *379*, 122317.

[7] S. M. Li, L. F. Tan, X. W. Meng, *Adv. Funct. Mater.* **2020**, 1908924.

[8] R. Khademi, D. Mohebbi-Kalhori, A. Razminia, *Int. J. Heat Mass Tran.* **2019**, *137*, 1001.

[9] X. J. Zhu, W. Feng, J. Chang, Y. W. Tan, J. C. Li, M. Chen, Y. Sun, F. Y. Li, *Nat. Commun.* **2016**, *7*, 10437.

[10] Z. Liu, K. Q. Qiu, X. X. Liao, T. W. Rees, Y. Chen, Z. Z. Zhao, L. N. Ji, H. Chao, *Chem. Commun.* **2020**, DOI: 10.1039.C9CC09728G.

[11] Y. C. Li, B. J. Chen, L. L. Tong, X. Z. Zhang, S. Xu, X. P. Li, J. S. Zhang, J. S. Sun, X. Wang, Y. Q. Zhang, G. Z. Sui, Y. H. Zhang, X. Q. Zhang, H. P. Xia, *Results Phys.* **2019**, *15*, 102704.

[12] E. C. Ximendes, U. Rocha, C. Jacinto, K. U. Kumar, D. Bravo, F. J. López, E. M. Rodríguez, J. García-Solé, D. Jaque, *Nanoscale* **2016**, *8*, 3057.

[13] H. Suo, X. Q. Zhao, Z. Y. Zhang, Y. F. Wu, C. F. Guo, *ACS Appl. Mater. Interfaces* **2018**, *10*, 39912.

[14] C. L. West, A. C. V. Doughty, K. Liu, W. R. Chen, *J. Bio-X Res.* **2019**, *2*, 159.

[15] U. Rocha, C. Jacinto, K. U. Kumar, F. J. López, D. Bravo, J. G. Solé, D. Jaque, *J. Lumin.* **2016**, *175*, 149.

[16] B. del Rosal, E. Carrasco, F. Ren, A. Benayas, F. Vetrone, F. Sanz-Rodríguez, D. Ma, Á. Juarranz, D. Jaque, *Adv. Funct. Mater.* **2016**, *26*, 6060.

[17] X. R. Deng, K. Li, X. C. Cai, B. Liu, Y. Wei, K. R. Deng, Z. X. Xie, Z. J. Wu, P. A. Ma, Z. Y. Hou, Z. Y. Cheng, J. Lin, *Adv. Mater.* **2017**, *29*, 1701266.

[18] B. del Rosal, A. Pérez-Delgado, E. Carrasco, D. J. Jovanović, M. D. Dramićanin, G. Dražić, Á. J. de la Fuente, F. Sanz-Rodriguez, D. Jaque, *Adv. Opt. Mater.* **2016**, *4*, 782.

[19] B. del Rosal, E. Ximendes, U. Rocha, D. Jaque, *Adv. Opt. Mater.* **2017**, *5*, 1600508.

[20] I. E. Kolesnikov, E. V. Golyeva, A. A. Kalinichev, M. A. Kurochkin, E. Lähderanta, M. D. Mikhailov, *Sensor. Actuat. B-Chem.* **2017**, *243*, 338.

[21] E. Carrasco, B. del Rosal, F. Sanz-Rodríguez, Á. J. de la Fuente, P. H. Gonzalez, U. Rocha, K. U. Kumar, C. Jacinto, J. G. Solé, D. Jaque, *Adv. Funct. Mater.* **2015**, *25*, 615.

[22] H. D. A. Santos, D. Ruiz, G. Lifante, C. Jacinto, B. H. Juarez, D. Jaque, *Nanoscale* **2017**, *9*, 2505.

[23] A. A. Kalinichev, M. A. Kurochkin, E. V. Golyeva, A. V. Kurochkin, E. Lähderanta, M. D. Mikhailov, I. E. Kolesnikov, *J. Lumin.* **2018**, *195*, 61.

[24] I. E. Kolesnikov, A. A. Kalinichev, M. A. Kurochkin, D. V. Mamonova, E. Yu. Kolesnikov, A. V. Kurochkin, E. Lähderanta, M. D. Mikhailov, *J. Lumin.* **2018**, *204*, 506.

[25] D. T. Delpy, M. Cope, *Phil. Trans. R. Soc. Lond. B* **1997**, *352*, 649.

[26] M. Miljković, B. Bird, M. Diem, *Analyst* **2012**, *137*, 3954.

[27] R. T. D. Peters, R. S. Hinks, R. M. Henkelman, *Magn. Reson. Med.* **1998**, *40*, 454.

[28] L. Marciniak, K. Trejgis, *J. Mater. Chem. C* **2018**, *6*, 7092.

[29] C. M. Gardner, S. L. Jacques, A. J. Welch, Proc. SPIE 1885, Advances in Fluorescence Sensing Technology, **1993.**
[30] H. Ding, B. Zhao, P. Baturin, F. Behroozi, S. Molloi, *Med. Phys.* **2014**, *41*, 101901.
[31] D. Ruiz, B. del Rosal, M. Acebrón, C. Palencia, C. Sun, J. Cabanillas-González, M. López-Haro, A. B. Hungría, D. Jaque, B. H. Juarez, *Adv. Funct. Mater.* **2017**, *27*, 1604629.
[32] X. J. Zhou, R. X. Wang, G. T. Xiang, S. Jiang, L. Li, X. B. Luo, Y. Pang, Y. L. Tian, *Opt. Mater.* **2017**, *66*, 12.
[33] M. Segev-Bar, N. Bachar, Y. Wolf, B. Ukrainsky, L. Sarraf, H. Haick, *Adv. Mater. Technol.* **2017**, *2*, 1600206.
[34] J. Yang, Y. X. Liu, Y. Y. Zhao, Z. Gong, M. Zhang, D. T. Yan, H. C. Zhu, C. G. Liu, C. S. Xu, H. Zhang, *Chem. Mater.* **2017**, *29*, 8119.
[35] H. Y. Zhou, M. Sharma, O. Berezin, D. Zuckerman, M. Y. Berezin, *ChemPhysChem* **2016**, *17*, 27.
[36] D. H. Ortgies, M. L. Tan, E. C. Ximendes, B. del Rosal, J. Hu, L. Xu, X. D. Wang, E. Martín Rodríguez, C. Jacinto, N. Fernandez, G. Chen, D. Jaque, *ACS Nano* **2018**, *12*, 4362.
[37] I. E. Kolesnikov, A. A. Kalinichev, M. A. Kurochkin, D. V. Mamonova, E. Yu. Kolesnikov, A. V. Kurochkin, E. Lähderanta, M. D. Mikhailov, *J. Lumin.* **2017**, *192*, 40.
[38] Y. Zhao, C. Riemersma, F. Pietra, R. Koole, C. de Mello Donegá, A. Meijerink, *ACS Nano* **2012**, *6*, 9058.
[39] Y. H. Cho, G. H. Gainer, A. J. Fischer, J. J. Song, S. Keller, U. K. Mishra, S. P. DenBaars, *Appl. Phys. Lett.* **1998**, *73*, 1370.
[40] D. K. Roper, W. Ahn, M. Hoepfner, *J. Phys. Chem. C* **2007**, *111*, 3636.
[41] S. Berciaud, L. Cognet, B. Lounis, *Phys. Rev. Lett.* **2008**, *101*, 077402.
[42] F. F. Zhou, D. Xing, Z. M. Ou, B. Y. Wu, D. E. Resasco, W. R. Chen, *J. Biomed. Opt.* **2009**, *14*, 021009.
[43] S. R. Ji, C. Liu, B. Zhang, F. Yang, J. Xu, J. Long, C. Jin, D. L. Fu, Q. X. Ni, X. J. Yu, *BBA-Rev. Cancer* **2010**, *1806*, 29.
[44] Z. Liu, J. T. Robinson, S. M. Tabakman, K. Yang, H. J. Dai, *Mater. Today* **2011**, *14*, 316.
[45] T. Hertel, S. Himmelein, T. Ackermann, D. Stich, J. Crochet, *ACS Nano* **2010**, *4*, 7161.
[46] A. K. Parchur, G. Sharma, J. M. Jagtap, V. R. Gogineni, P. S. LaViolette, M. J. Flister, S. B. White, A. Joshi, *ACS Nano* **2018**, *12*, 6597.
[47] V. P. Pattani, J. W. Tunnell, *Lasers Surg. Med.* **2012**, *44*, 675.
[48] G. S. Terentyuk, A. V. Ivanov, N. I. Polyanskaya, I. L. Maksimova, A. A. Skaptsov, D. S. Chumakov, B. N. Khlebtsov, N. G. Khlebtsov, *Quantum Electron.* **2012**, *42*, 380.
[49] H. F. Wang, T. B. Huff, D. A. Zweifel, W. He, P. S. Low, A. Wei, J. X. Cheng, *PNAS* **2005**, *102*, 15752.
[50] M. Chen, X. L. Fang, S. H. Tang, N. F. Zheng, *Chem. Commun.* **2012**, *48*, 8934.
[51] K. M. Au, Z. Lu, S. J. Matcher, S. P. Armes, *Adv. Mater.* **2011**, *23*, 5792.
[52] S. C. Pu, M. J. Yang, C. C. Hsu, C. W. Lai, C. C. Hsieh, S. H. Lin, Y. M. Cheng, P. T. Chou, *Small* **2006**, *2*, 1308.
[53] M. Q. Chu, X. J. Pan, D. Zhang, Q. Wu, J. L. Peng, W. X. Hai, *Biomaterials* **2012**, *33*, 7071.
[54] B. Galindo, A. Benedito, E. Gimenez, V. Compañ, *Compos. B. Eng.* **2016**, *98*, 330.
[55] A. Burke, X. Ding, R. Singh, R. A. Kraft, N. Levi-Polyachenko, M. N. Rylander, C. Szot, C. Buchanan, J. Whitney, J. Fisher, H. C. Hatcher, R. D'Agostino, N. D. Kock, P. M. Ajayan, D. L. Carroll, S. Akman, F. M. Torti, S. V. Torti, *PNAS* **2009**, *106*, 12897.
[56] C. Ni, P. R. Bandaru, *Carbon* **2009**, *47*, 2898.
[57] Y. B. Li, G. X. Bai, S. J. Zeng, J. H. Hao, *ACS Appl. Mater. Interfaces* **2019**, *11*, 4737.

[58] S. Kalytchuk, K. Poláková, Y. Wang, J. P. Froning, K. Cepe, A. L. Rogach, R. Zbořil, *ACS Nano* **2017**, *11*, 1432.
[59] L. Cao, X. Wang, M. J. Meziani, F. S. Lu, H. F. Wang, P. G. Luo, Y. Lin, B. A. Harruff, L. M. Veca, D. Murray, S. Y. Xie, Y. P. Sun, *J. Am. Chem. Soc.* **2007**, *129*, 11318.
[60] B. Liu, C. X. Li, B. G. Xing, P. P. Yang, J. Lin, *J. Mater. Chem. B* **2016**, *4*, 4884.
[61] S. Sekiyama, M. Umezawa, S. Kuraoka, T. Ube, M. Kamimura, K. Soga, *Sci. Rep.* **2018**, *8*, 16979.
[62] U. Rocha, K. U. Kumar, C. Jacinto, I. Villa, F. Sanz-Rodríguez, M. del Carmen Iglesias de la Cruz, A. Juarranz, E. Carrasco, F. C. J. M. van Veggel, E. Bovero, J. G. Solé, D. Jaque, *Small* **2014**, *10*, 1141.
[63] U. Rocha, C. Jacinto da Silva, W. Ferreira Silva, I. Guedes, A. Benayas, L. Martínez Maestro, M. Acosta Elias, E. Bovero, F. C. J. M. van Veggel, J. A. García Solé, D. Jaque, *ACS Nano* **2013**, *7*, 1188.
[64] B. del Rosal, I. Villa, D. Jaque, F. Sanz-Rodríguez, *J. Biophoton* **2016**, *9*, 1059.
[65] H. Yuan, C. G. Khoury, C. M. Wilson, G. A. Grant, A. J. Bennett, T. Vo-Dinh, *Nanomedicine.* **2012**, *8*, 1355.
[66] H. Xie, B. Goins, A. Bao, Z. Wang, W. Phillips, *Int. J. Nanomed.* **2012**, 2227.
[67] T. Thestrup, J. Litzlbauer, I. Bartholomäus, M. Mues, L. Russo, H. Dana, Y. Kovalchuk, Y. Liang, G. Kalamakis, Y. Laukat, S. Becker, G. Witte, A. Geiger, T. Allen, L. C. Rome, T.-W. Chen, D. S. Kim, O. Garaschuk, C. Griesinger, O. Griesbeck, *Nat. Methods.* **2014**, *11*, 175.
[68] D. P. O'Neal, L. R. Hirsch, N. J. Halas, J. D. Payne, J. L. West, *Cancer Letters* **2004**, *209*, 171.
[69] G. S. Terentyuk, G. N. Maslyakova, L. V. Suleymanova, N. G. Khlebtsov, B. N. Khlebtsov, G. G. Akchurin, I. L. Maksimova, V. V. Tuchin, *J. Biomed. Opt.* **2009**, *14*, 021016.
[70] M. Ma, H. Chen, Y. Chen, X. Wang, F. Chen, X. Cui, J. Shi, *Biomaterials* **2012**, *33*, 989.
[71] W. W. Overwijk, N. P. Restifo, *Current Protocols in Immunology* **2000**, *39*,20(1-29).
[72] J. McK. Snowden, P. E. Bouton, P. V. Harris, *J. Food Science* **1977**, *42*, 890.
[73] M. M. Ogle, A. D. Smith McWilliams, M. J. Ware, S. A. Curley, S. J. Corr, A. A. Martí, *J. Phys. Chem. B* **2019**, *123*, 7282.
[74] H. D. A. Santos, E. C. Ximendes, M. del C. I. la Cruz, I. Chaves-Coira, B. del Rosal, C. Jacinto, L. Monge, I. Rubia-Rodríguez, D. Ortega, S. Mateos, J. GarcíaSolé, D. Jaque, N. Fernández, *Adv. Funct. Mater.* **2018**, *28*, 1803924
[75] A. Doughty, A. Hoover, E. Layton, C. Murray, E. Howard, W. Chen, *Materials* **2019**, *12*, 779.

Supporting Information

Ag_2S nanoheaters with advanced multiparameter sensing for reliable thermal feedback during *in vivo* tumour therapy

Yingli Shen*, Harrisson Santos*, Erving Ximendes,* Jose Lifante-Cañavate, Ana Sanz-Portilla, Luis Monge, Nuria Fernández, Carlos Jacinto,Carlos Brites, Luis Dias Carlos, Antonio Benayas, M. Carmen Iglesias-de la Cruz, and Daniel Jaque.

Section S1 Physical characterizations of Ag_2S NPs

The physical of Ag_2S NPs we used for our work including the X-ray diffraction (XRD), transmission electron telescope (TEM) image and the size-distribution analysis, as shown in **Figure S1 (a)-(c)**. The XRD result revealed Ag_2S NPs are monoclinic phase, which in accordance with JCPD No. 140072, in turns, possess a good quality of crystallinity. **Figure S1(b)** shows an uniform and spherical morphology of Ag_2S NPs with an average size around 5 nm according to the size distribution graph (**Figure S1(c)**).

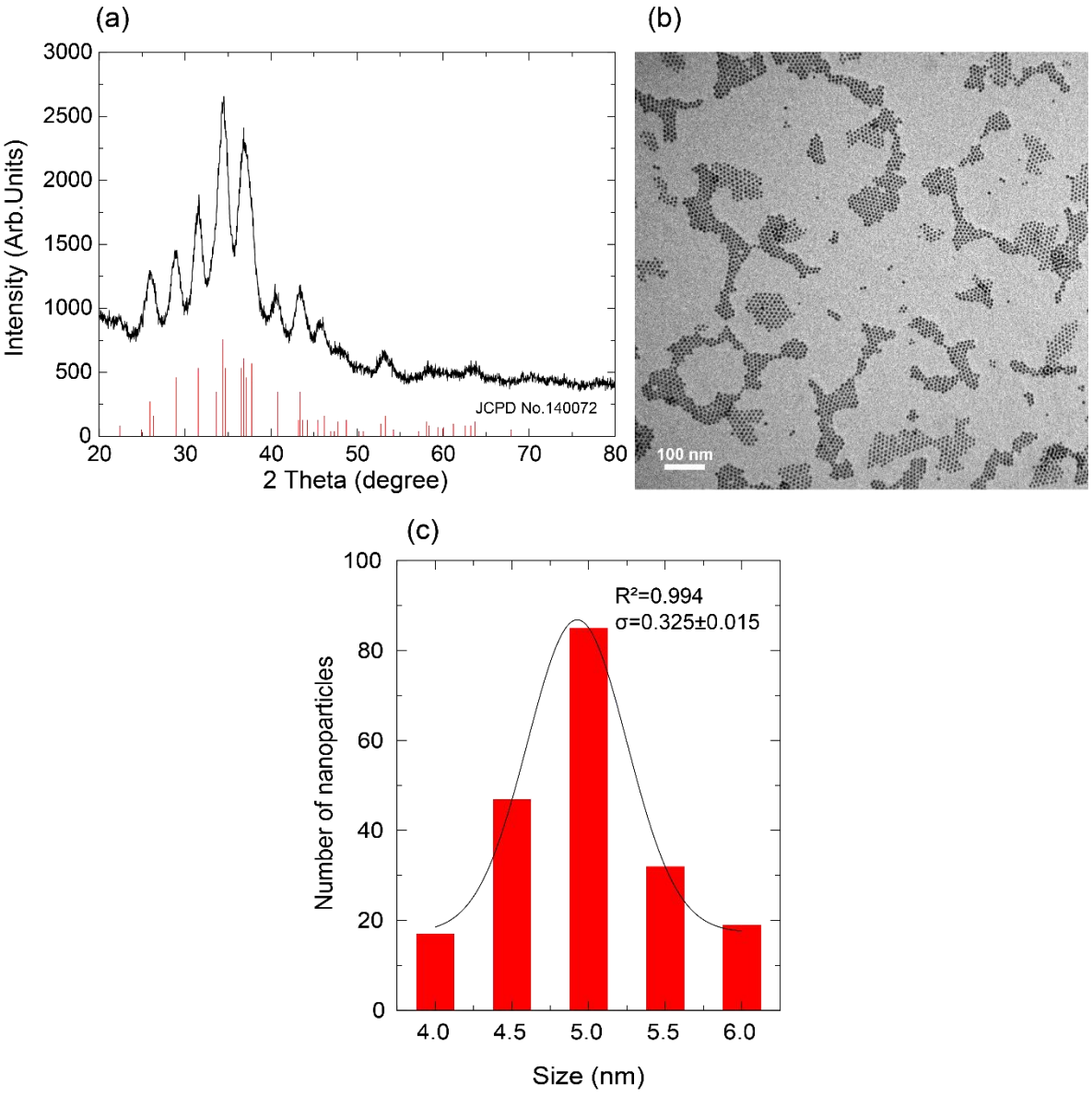

Figure S1 (a) XRD pattern of Ag_2S NPs, **(b)** TEM image of Ag_2S NPs dispersed in water with a scale bar at 100 nm, and **(c)** size distribution of Ag_2S NPs obtained from **(b)** after measuring 200 NPs' size.

Section S2 Relationship between laser power densities and temperature increments of Ag_2S NPs aqueous solution

To estimate the heating ability of Ag_2S NPs in water, we investigated the relationship between temperature increments and laser power densities through using a thermal camera to monitor the temperature change of the solution dynamically, then we could obtain the stable temperature of solution related to each laser power density. As the results, it showed a perfect proportional relation between them, which reveals the heating capability of Ag_2S NPs.

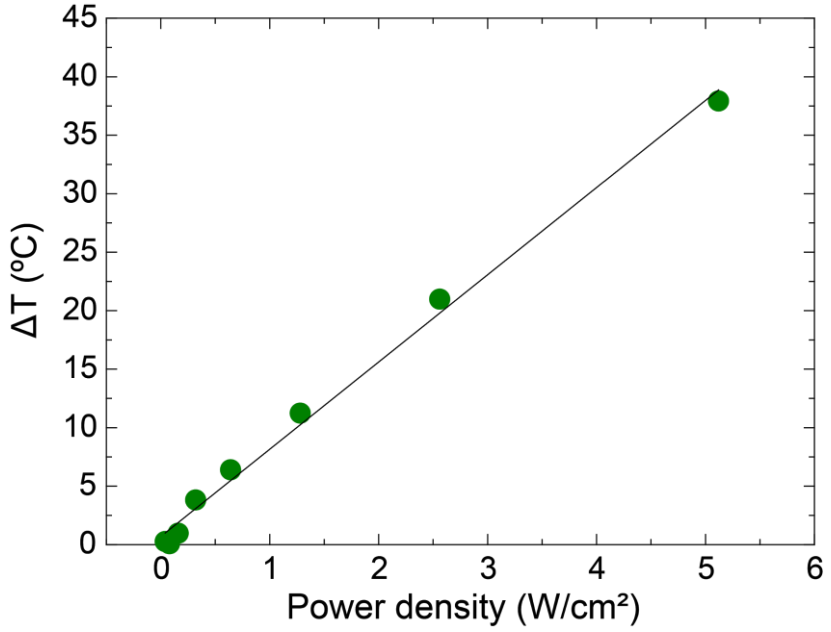

Figure S2 Temperature increments trend of Ag_2S NPs under different laser power densities excitation.

Section S3 Quantum yield (QY) variation trend of Ag_2S NPs according to temperature

Here we need to include the data from Luis Carlos. Data on the temperature dependence of QY would be included in a separate work.

Section S4 Deducing process of Eq. 5

The light-to-heat conversion efficiency (η_h) of the quantum dots (QDs) could be defined as the percentage of the absorbed pump power that transformed into heat through the non-radiative decay process, while the absolute quantum yield (QY) is determined by the radiative decay process. Thus, in turns, predestine the close relationship between η_h and QY. According to the previous related work then extended to QDs situation, [1,2] the calculation expression of η_h could be written as below:

$$\eta_h=1-\eta_p[QY \times (\lambda_p/\lambda_{em})]$$

(Eq. S1)

where η_{exc} is the pump quantum efficiency, QY is the radiative quantum efficiency of the Ag_2S NPs (*i.e.* quantum yield, use QY directly here), λ_{exc} is the wavelength of the pump power, λ_{em} is the average fluorescence photon wavelength. Here, we make the related assumptions: i) the only reason caused the pump quantum efficiency lower is the presence of non-radiative sites; ii) the only reasons caused the QY to become lower are the concentration quenching and presence of multiphoton non-radiative decay process. According to the assumptions, under the no laser extraction circumstance (*i.e.* only have the fluorescence quantum defection), η_p=1. Then substitute the value into Eq. S1, the equation could be simplified as:

$$\eta_h=1-QY \times (\lambda_p/\lambda_{em})$$

which is the **Eq. 5** in the text.

Section S5 - *In Vivo* fluorescence images during tumor treatment induced by sufficient treatment (Ag_2S+laser)

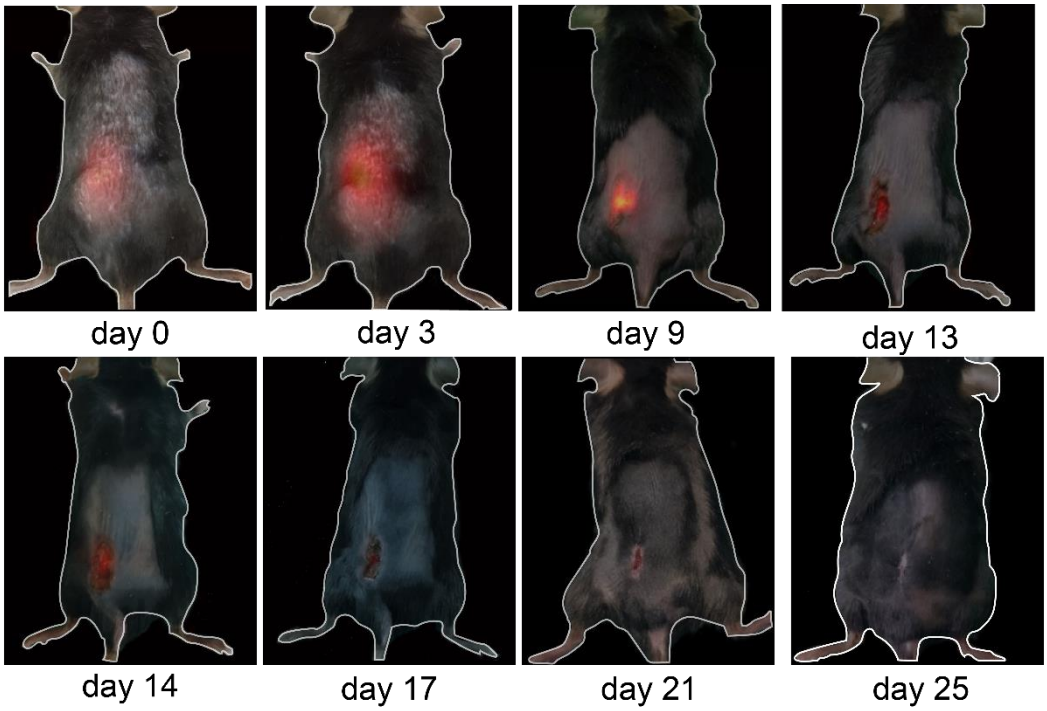

Figure S4 *In vivo* fluorescence images through the tumor treatment process. The optical photo was took exactly after the inoculation, then the time-evolution fluorescence images were obtained by a Xenics NIR-II camera (XEVA-9600) during the following 25 days, while day 0 means the same day of inoculation. The tumor location was indicated by a red circle in the optical photo.

Section S6 Experimental setup of emission spectra generated by Ag_2S NPs within tumor

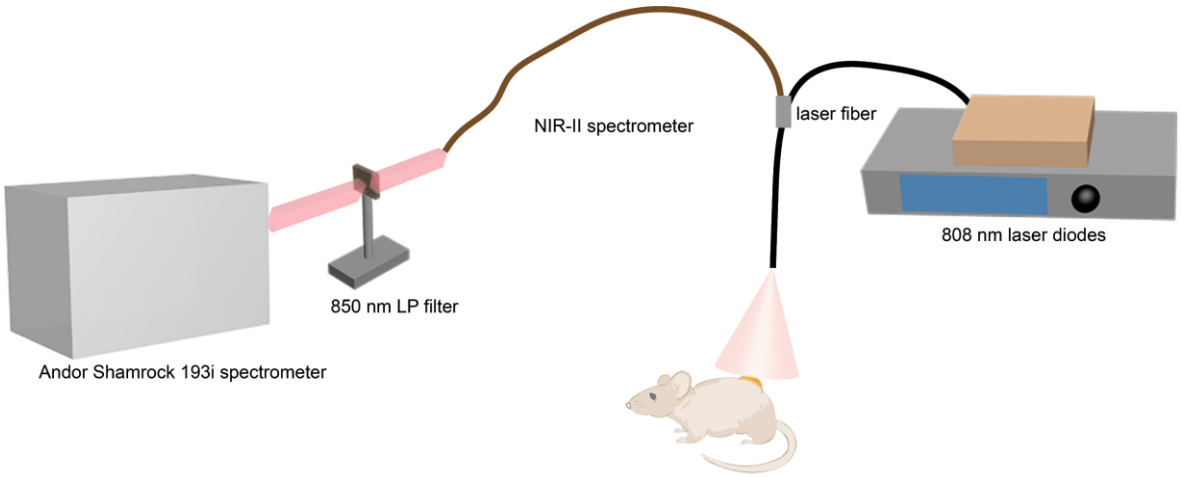

Figure S5 Experimental setup for obtaining the spectra generated by Ag_2S NPs within tumor. During the process, we used a multimode fiber which combined the excited fibre with NIR-II spectrometer, thereby we could monitor the real-time spectra of Ag_2S NPs within the tumor when we excited it. After the NIR-II spectrometer collecting the signal of Ag_2S NPs then pass through a 850 nm LP filter (long-pass, Thronlab, Inc.) to remove the signal of laser, it will be analyzed by the Andor Shamrock 193i spectrometer to obtain the spectra finally.

Section S7 Spectra comparison of Ag_2S NPs with and without tumor at higher temperatures

The spectra without tumor were obtained from Ag_2S NPs solution in a cuvette, while the spectra with tumor were taken from a tumor-bearing mouse at the tumor site according to the experimental setup illustrated in **Section S6.** With the 808 nm laser excitation, the temperature of both systems increased because of the Ag_2S NPs heating. Moreover, the noise of spectra became obviously due to the luminescence intensity of Ag_2S NPs decreased induced by the thermal quenching. As shown in **Figure S6**, the spectral distortions area induced by tumor were evidential below 1150 nm at all temperature conditions, which, in turns, evoke the importance of distinguishing the distortions of spectra induced by tumor or the temperature effect.

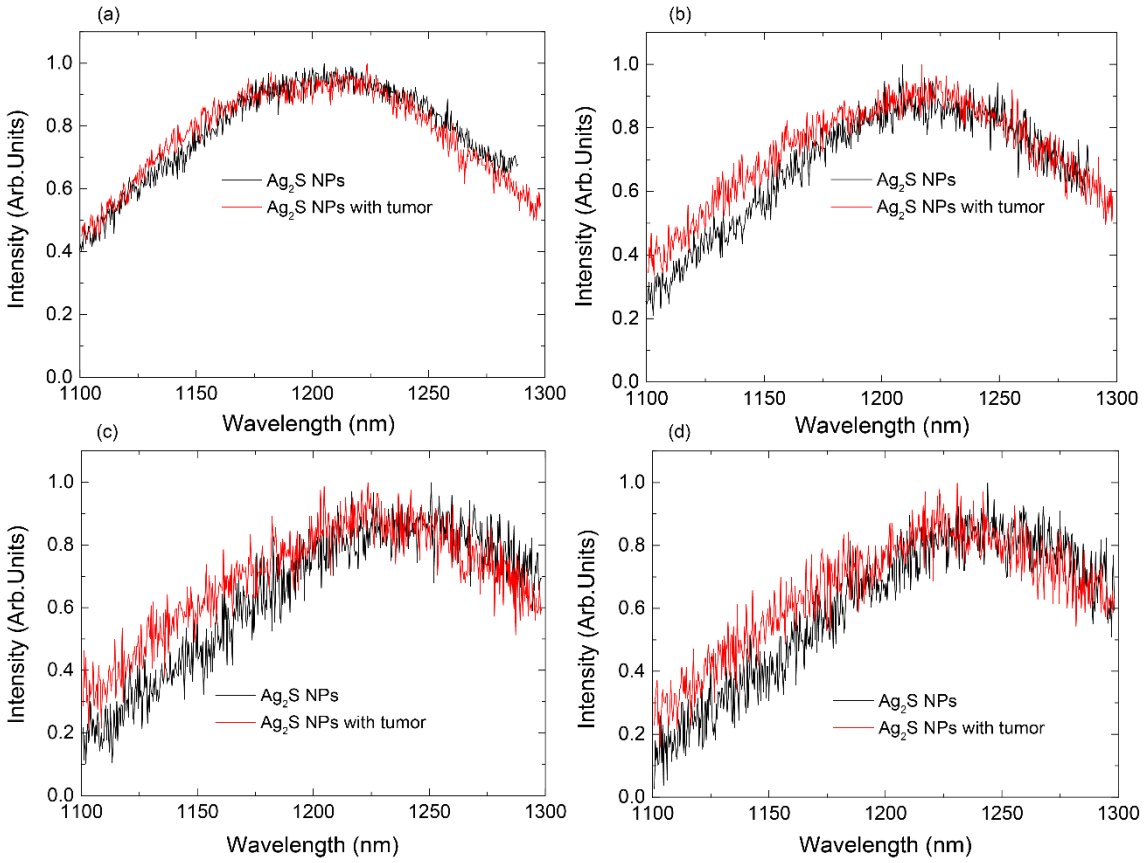

Figure S6 Spectra comparison of Ag_2S NPs with and without tumor at different temperatures: (a) 42 ºC, (b) 52 ºC, (c) 62 ºC, and (d) 65 ºC.

Section S8 – Optical properties and multiparametric thermal readouts

Let ρ_1 and ρ_2 be two different thermometric parameters. S_{ρ_1} and S_{ρ_2} are their corresponding relative thermal sensitivities (as measured in the absence of any tissue). If a tissue is found in the path of the light (emitted by the nanothermometer) to the detection system, then the thermal dependence of the optical properties of that tissue are going to change these sensitivities in amounts of ΔS_{ρ_1} and ΔS_{ρ_2}, respectively [REF: Possible ACS Nano]. By using the definition of the relative thermal sensitivity for the detected signal and Leibniz's notation for infinitesimal changes, the following equations should necessarily hold:

$$S_{\rho_1} + \Delta S_{\rho_1} = \frac{1}{\rho_1}\left|\frac{d\rho_1}{dT}\right| \Leftrightarrow |dT| = \frac{1}{S_{\rho_1} + \Delta S_{\rho_1}}\frac{|d\rho_1|}{\rho_1}$$

(Eq. S2)

$$S_{\rho_2} + \Delta S_{\rho_2} = \frac{1}{\rho_2}\left|\frac{d\rho_2}{dT}\right| \Leftrightarrow |dT| = \frac{1}{S_{\rho_2} + \Delta S_{\rho_2}}\frac{|d\rho_2|}{\rho_2}$$

(Eq. S3)

Since the temperature variation should be the same independently of the thermometric parameter selected to sense it, then Eq. S1 and S2 result in:

$$\frac{1}{S_{\rho_1} + \Delta S_{\rho_1}}\frac{|d\rho_1|}{\rho_1} = \frac{1}{S_{\rho_2} + \Delta S_{\rho_2}}\frac{|d\rho_2|}{\rho_2}$$

(Eq. S4)

Equation S3, therefore, establishes that multiparametric thermal sensing will only converge in *in vivo* experiments if the effects induced by changes in the optical properties of tissues are being considered. When discussing Figure 5d in the main text, however, it was observed that by a cautious selection of the thermometric parameters, one can satisfy the following equality:

$$\frac{1}{S_{\rho_1}}\frac{|d\rho_1|}{\rho_1} = \frac{1}{S_{\rho_2}}\frac{|d\rho_2|}{\rho_2}$$

(Eq. S5)

i.e., the temperature variation as estimated by the relative changes in the detected parameters agree between themselves when considering only their intrinsic thermal sensitivities (measured without any tissue). In order to understand what this means, one needs to insert S4 (a particular condition) into S4 (a general rule). One will find that:

$$\Delta S_{\rho_2}\frac{|d\rho_1|}{\rho_1} = \Delta S_{\rho_1}\frac{|d\rho_2|}{\rho_2}$$

(Eq. S6)

Since $|d\rho_1|$ and $|d\rho_2|$ are arbitrary infinitesimal changes, this means that only one of the following two equations is true:

$$\Delta S_{\rho_1} = \Delta S_{\rho_2} = 0$$

(Eq. S7.1)

or

$$\frac{1}{\Delta S_{\rho_1}} \frac{|d\rho_1|}{\rho_1} = \frac{1}{\Delta S_{\rho_2}} \frac{|d\rho_2|}{\rho_2}$$

(Eq. S7.2)

The first of them (Eq. S6.1) means that the thermometric parameters were so well selected that the thermal dependence of the optical properties of the tissue were completely avoided. The second possibility, on the other hand, indicates that the tissue-induced effects are still affecting the measurement but having equal contributions on the estimation of ΔT by the different thermometric parameters.

Section S9 Temperature variation trend with mouse tissue and tumor

We obtained the time-evolution temperature variation at different sites of mouse as shown in **Figure S7 (a)-(c).** Then we did a non-curve fitting for the three circumstances according to the following equation:

$$T = A - Bexp(-t/\tau_0)^{\beta}$$

(Eq. S8)

Where A and B are the constant parameters, repspectively, τ_0 is the relaxation time (s), and β is a parameter to evaluate the deviation level from the fully exponential growth.

After defining the **Eq. S8**, we operated the fitting and got the values for different constants and parameters as well as the R^2 under different situations. That are: for intratumoral case, the values are A = 39.59, B = 39.45, τ_0 = 61.98 s, β = 0.642 and R^2 = 0.9978 (**Figure S7 (a)**). Then for surface+NPs case, the values are A = 22.58, B = 21.12, τ_0 = 66.39 s, β = 0.96822 and R^2 = 0.999737 (**Figure S7 (b)).** Lastly for surface case, the values are A = 9, .00, B = 9.39, τ_0 = 43.97 s, β = 0.710263 and R^2 = 0.999855 (**Figure S7 (c)).** As mentioned before, the value of β indicates the deviation level from the fully exponential growth, namely only when β = 1 showed the curve obey exponential growth, otherwise it didn't follow an exponential trend. Regarding the fitting results we obtained, all the values of R^2 were nearly 1 which showed a good fitting property of Eq. S8, in turn, these time-evolution temperature trends didn't obey the exponential growth with time increasing because of the tissues properties affection.

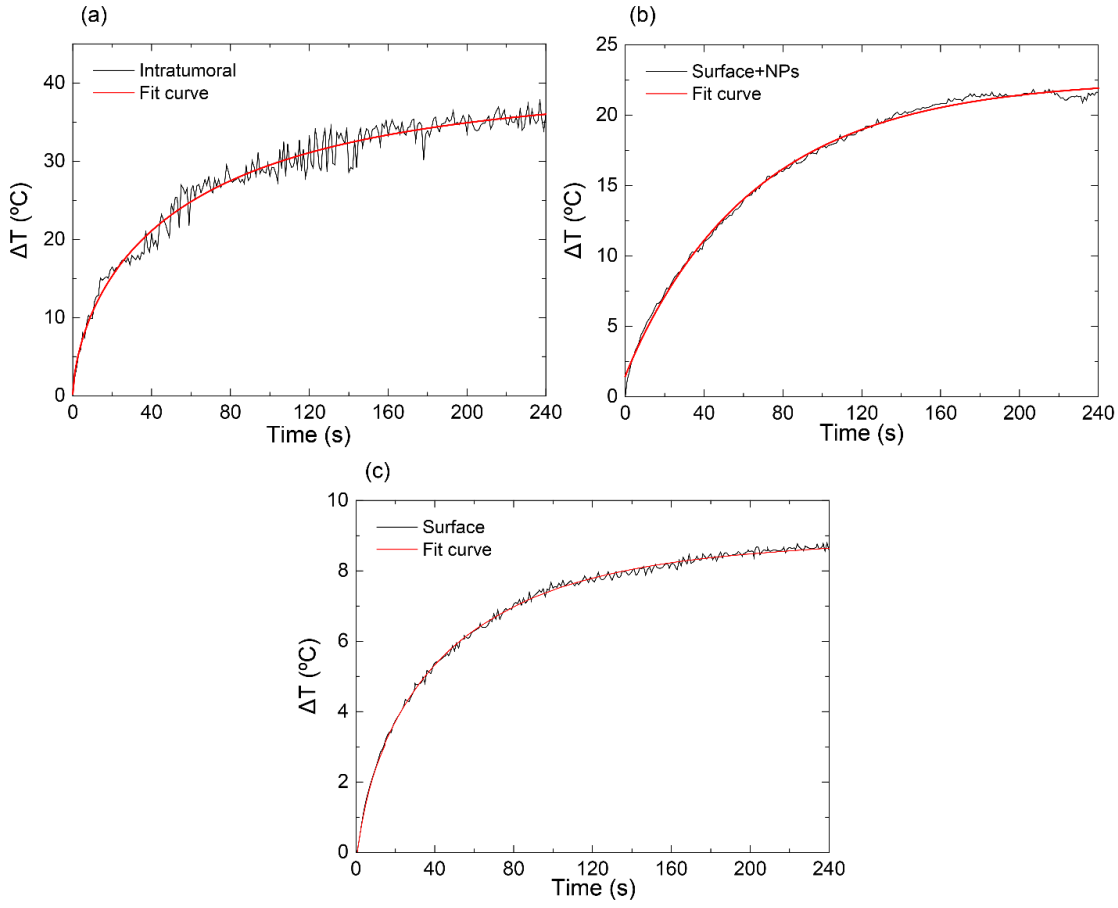

Figure S7 Time-evolution temperature variation trend at different sites of mouse and its non-exponential fitting curve: (a) intratumoral, (b) surface+NPs and (c) surface, while the black curves are the experimental results and red curves are fitting results.

Section S10 - Optical photos of insufficient treatments of tumor

The optical photos of tumor-bearing mice were applied with the insufficient treatments, which are only injected with Ag_2S NPs (a) and only illuminated by laser (b), as contrasts with the sufficient treatment (Ag_2S+laser). With the insufficient treatments, the tumor volume increased rapidly and bleeding and necrosis showed, then we have to sacrificed them around day 17.

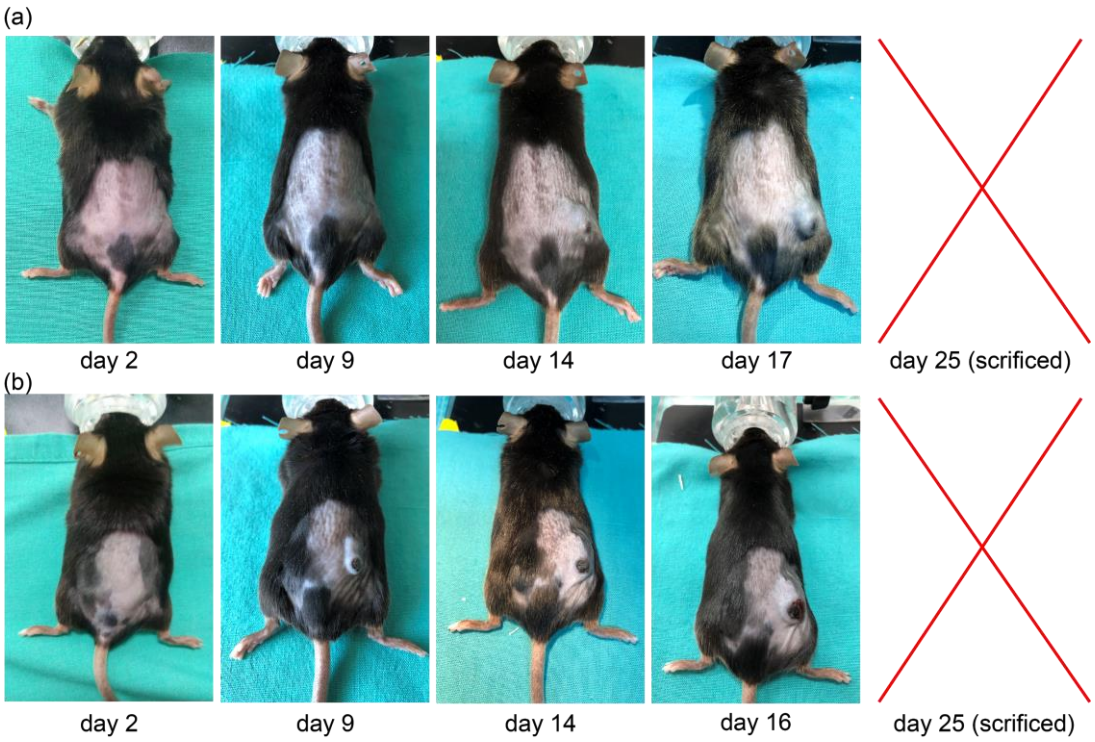

Figure S8 Optical photos of (a) a tumor-bearing mouse only subjected Ag_2S NPs and (b) a tumor-bearing mouse only treated with the 808 nm laser at 1 W/cm^2. Since the tumor of the mouse only treated with laser started to bleed and became greatly ulcerated at day 16, we proceeded to sacrifice it at day 16.